

**Fast-neutron-induced fission cross section of Pu(242) measured at the neutron time-of-flight facility nELBE**

Kögler, T.; Junghans, A. R.; Beyer, R.; Dietz, M.; Düllmann, C. E.; Eberhardt, K.; Lorenz, C.; Müller, S. E.; Nolte, R.; Reinhardt, T. P.; Schmidt, K.; Runke, J.; Schwengner, R.; Takacs, M.; Vascon, A.; Wagner, A.;

Originally published:

February 2019

**Physical Review C 99(2019)2, 024604**

DOI: <https://doi.org/10.1103/PhysRevC.99.024604>

Perma-Link to Publication Repository of HZDR:

<https://www.hzdr.de/publications/Publ-28878>

Release of the secondary publication  
on the basis of the German Copyright Law § 38 Section 4.

# Fast-neutron-induced fission cross section of $^{242}\text{Pu}$ measured at $n\text{ELBE}$

T. Kögler,<sup>1,2,\*</sup> A. R. Junghans,<sup>1,\*</sup> R. Beyer,<sup>1</sup> M. Dietz,<sup>1,2,†</sup> Ch. E. Düllmann,<sup>3,4,5</sup>  
K. Eberhardt,<sup>3,4</sup> Ch. Lorenz,<sup>1,2,‡</sup> S. E. Müller,<sup>1</sup> R. Nolte,<sup>6</sup> T. P. Reinhardt,<sup>1,2</sup>  
K. Schmidt,<sup>1,2,§</sup> J. Runke,<sup>3,5</sup> R. Schwengner,<sup>1</sup> M. Takacs,<sup>1,2</sup> A. Vascon,<sup>1,3,¶</sup> and A. Wagner<sup>1</sup>

<sup>1</sup>*Helmholtz-Zentrum Dresden - Rossendorf, 01328 Dresden, Germany*

<sup>2</sup>*Technische Universität Dresden, 01062 Dresden, Germany*

<sup>3</sup>*Institute of Nuclear Chemistry, Johannes Gutenberg University Mainz, 55099 Mainz, Germany*

<sup>4</sup>*Helmholtz-Institut Mainz, 55099 Mainz, Germany*

<sup>5</sup>*SHE Chemistry Department, GSI Helmholtzzentrum für Schwerionenforschung GmbH, 64291 Darmstadt, Germany*

<sup>6</sup>*Physikalisch-Technische Bundesanstalt, 38116 Braunschweig, Germany*

(Dated: October 29, 2018)

The fast-neutron-induced fission cross section of  $^{242}\text{Pu}$  was measured at the neutron time-of-flight facility  $n\text{ELBE}$ . A parallel-plate fission ionization chamber with novel, homogeneous, large-area  $^{242}\text{Pu}$  deposits on Si-wafer backings was used to determine this quantity relative to the IAEA neutron cross-section standard  $^{235}\text{U}(n,f)$  in the energy range of 0.5 to 10 MeV. The number of target nuclei was determined from the measured spontaneous fission rate of  $^{242}\text{Pu}$ . This helps to reduce the influence of the fission fragment detection efficiency on the cross section. Neutron transport simulations performed with Geant4, MCNP6 and Fluka 2011 are used to correct the cross-section data for neutron scattering. In the reported energy range the systematic uncertainty is below 2.7 % and on average the statistical uncertainty is 4.9 %. The determined results show an agreement within 0.67(16) % to recently published data and a good accordance to current evaluated data sets.

## I. INTRODUCTION

Future nuclear power concepts with a closed fuel cycle, such as accelerator driven systems and generation IV reactors, targeted to use their fuel more efficiently, will produce less radioactive waste, meet the stringent standards of safety and proliferation resistance, and strive to be more economically competitive [1] compared to current reactor designs. Transmutation of nuclear waste in fast reactors is discussed as a way to reduce the radiotoxicity of the presently existing nuclear fuel. However, the technical realization of such plants is a challenging and expensive endeavour. Accurate nuclear data, especially fast-neutron-induced fission cross sections, are essential for new reactor designs.

$^{242}\text{Pu}$  is the longest-lived plutonium isotope in spent nuclear fuel ( $T_{1/2} = 375,000$  yr [2]) and hence important for nuclear transmutation, as  $^{244}\text{Pu}$  production is negligible [3].

Current uncertainties of the  $^{242}\text{Pu}(n,f)$  cross section are of about 21 % in the energy range from 0.5 to 2.23 MeV [4]. For a reliable prediction of the neutron multiplication and other reactor core parameters in these novel reactor concepts, the total uncertainty needs to be

reduced to below 5 % [4, 5]. This task is addressed within the INDEN project [6], where  $^{242}\text{Pu}$  is one of the nuclides with the highest priority.

The fast neutron-induced fission of  $^{242}\text{Pu}$  is studied since 1960 [7]. A brief summary of the available experimental data acquired since then has already been given in Ref. [8]. In addition, an absolute measurement of the fission cross section was also performed in Dresden in 1983 by using quasi-monoenergetic neutrons with energies of 2.6 MeV, 8.4 MeV and 14.7 MeV [9]. Recently published measurements done at the Los Alamos National Laboratory by Tovesson *et al.* [10], at the Joint Research Center Geel by Salvador-Castineira *et al.* [8] and at the National Physical Laboratory of the United Kingdom in Teddington by Matei *et al.* [11] and Marini *et al.* [12] tend to be lower than present evaluated nuclear data [13]. To reduce the total uncertainty of the evaluated fission cross-section, more accurate and precise nuclear data over a large energy range is needed.

This challenging task was addressed at the neutron time-of-flight (ToF) facility  $n\text{ELBE}$  of the Center for High-Power Radiation Sources ELBE<sup>1</sup> at Helmholtz-Zentrum Dresden - Rossendorf.  $n\text{ELBE}$  is the first photo-neutron source at a superconducting electron accelerator. It allows operating the electron beam in continuous-wave (cw) mode with more than 100 kHz micropulse repetition rate. Improved neutron beam intensity, experimental conditions, e.g. a low scattering environment, and a suitable spectral fluence for fast neutron-induced reaction studies provided first-rate conditions to achieve this aim [14].

\* Corresponding author: t.koegler@hzdr.de, a.junghans@hzdr.de

† Present address: The University of Edinburgh, Edinburgh EH8 9YL, UK

‡ Present address: Lund University, P.O. Box 117, 221 00 Lund, Sweden

§ Present address: Michigan State University, 220 Trowbridge Rd East Lansing, MI 48824, USA

¶ Present address: ERAMET Research, 1 avenue Albert Einstein - B.P. 120 - F-78193 Trappes Cedex, France

<sup>1</sup> Electron Linac for beams with high Brilliance and low Emittance

66 The present work reports an experiment on the neu-  
67 tron-induced fission cross section of  $^{242}\text{Pu}$  relative to the  
68 IAEA neutron cross-section standard  $^{235}\text{U}(\text{n},\text{f})$  [15].

## 69 II. EXPERIMENTAL SETUP

### 70 A. Fast neutrons at ELBE

71 The  $n\text{ELBE}$  photo-neutron source [16–18] produces  
72 fast neutrons with kinetic energies between 10 keV and  
73 20 MeV. Electrons impinging on a liquid lead target  
74 produce bremsstrahlung during their deceleration. This  
75 bremsstrahlung generates the neutrons via  $(\gamma, \text{n})$  reac-  
76 tions on the lead nuclei. The neutrons, in turn, are emit-  
77 ted almost isotropically from the radiator, while a large  
78 part of the electrons and the bremsstrahlung photons  
79 mainly emerge in the forward direction. To minimize the  
80 photon-to-neutron ratio, only neutrons emitted through  
81 under  $100^\circ$  are used in the experimental area passing a  
82 dedicated collimator system. The excellent timing of the  
83 ELBE electron beam of  $\sim 5$  ps pulse length in combina-  
84 tion with the compactness of the neutron source, enables  
85 high resolution neutron time-of-flight experiments even  
86 at short flight paths of around 6 m.

87 The present experiment was performed with an elec-  
88 tron beam energy of 30 MeV and an average bunch charge  
89 of 73 pC on the neutron-producing target. The repetition  
90 rate was 406.25 kHz. The corresponding pulse separation  
91 of  $2.46 \mu\text{s}$  prevents neutron pulse overlap while still pro-  
92 viding a beam intensity of  $3.7 \cdot 10^4 \text{ n}/(\text{cm}^2\text{s})$  which is suf-  
93 ficient for the present experiment. An absorber reducing  
94 the  $\gamma$ -flash of the electron beam in this experiment was  
95 not required.

### 96 B. Fission chambers

97 A parallel-plate plutonium fission ionization chamber  
98 (hereafter PuFC) was constructed at HZDR [19, 20]. It  
99 is equipped with eight large area ( $\varnothing$  74 mm), isotopic  
100 pure (cf. Tab. I), thin (96(3) to 126(4)  $\mu\text{g}/\text{cm}^2$ ) and  
101 homogeneous deposits of  $^{242}\text{Pu}$ , which have been pro-  
102 duced within the TRAKULA project by Vascon *et al.*  
103 [21] at the Institute of Nuclear Chemistry of the Johannes  
104 Gutenberg University Mainz. Molecular plating was used  
105 to precipitate the fissile material from a nitrate solution  
106 on titanium coated silicon wafers of 400  $\mu\text{m}$  thickness.  
107 Due to the flatness and minimal surface roughness of the  
108 Si-wafers, homogeneous thin layers containing plutonium  
109 could be produced. SEM/EDX measurements of the sur-  
110 face of the  $^{242}\text{Pu}$  layers revealed cracks on a  $< 1 \mu\text{m}$  scale,  
111 which are due to the drying of the isopropanol solvent  
112 used in the molecular plating. Nevertheless, the homo-  
113 geneity is still better than for conventional deposition  
114 (e.g. painting or electro-deposition) on metallic foils.

115 The incident neutron flux of the reported experiment  
116 was determined by the well characterized  $^{235}\text{U}$  trans-

TABLE I. Isotopic composition of the used plutonium targets in the PuFC and uranium targets in the H19. The tabulated values for uranium have been picked from Ref. [22]. The plutonium composition (Batch I.D. Pu-242-327A1) was given by the manufacturer, Oak Ridge National Laboratory (ORNL).

PuFC		Abundance / %	
		H19	
$^{238}\text{Pu}$	0.0020(3)	$^{234}\text{U}$	0.03620(20)
$^{239}\text{Pu}$	0.0050(3)	$^{235}\text{U}$	99.9183(3)
$^{240}\text{Pu}$	0.0220(3)	$^{236}\text{U}$	0.00940(10)
$^{241}\text{Pu}$	0.0020(3)	$^{238}\text{U}$	0.03610(20)
$^{242}\text{Pu}$	99.9670(3)		
$^{244}\text{Pu}$	0.0020(3)		

117 fer instrument H19 of PTB Braunschweig [22, 23]. An  
118 overview of the key-properties of the fission targets of  
119 both fission chambers is given in Tab. II.

TABLE II. Key parameters of the PuFC and H19 fission deposits. The areal densities and total activity of the  $n\text{ELBE}$  targets have been calculated from their individual spontaneous fission rates, which have been measured in situ and reduce the systematic uncertainties compared to conventional  $\alpha$ -spectroscopy (see Sec. II E for more details.) Their homogeneity was derived from radiographic images. The properties of the H19 fission deposits were taken from Refs. [22, 23].

	PuFC ( $^{242}\text{Pu}$ )	H19 ( $^{235}\text{U}$ )
type of deposition	molecular plating	painting
no. of deposits	8 (single-sided)	5 (double-sided)
deposited area / $\text{cm}^2$	43.0(5)	45.4(5)
enrichment / %	99.9670(3)	99.9183(3)
total mass / mg	37.24(22)	201.4(5)
areal density / $\mu\text{g}/\text{cm}^2$	96(3)-126(4)	444(5)
total activity <sup>a</sup> / kBq	8,317.60	32.91
homogeneity / %	96.7 <sup>b</sup>	>96

<sup>a</sup> Including contaminants.

<sup>b</sup> Homogeneity means 1 minus the ratio of the standard deviation and the mean of the summed intensities of the radiographic images.

120 Both H19 and PuFC were operated in the forward  
121 biasing mode. This means that the five double-sided  
122 fission samples of the H19 and the eight single-sided  
123 samples of the PuFC were cathodes on ground poten-  
124 tial. Compared to the H19 electrode spacing of 5 mm,  
125 the distance between the anodes and cathodes of the  
126 PuFC was doubled, to increase the signal-to-noise ratio  
127 (charge of fission fragment induced signals compared to  
128 the charge of  $\alpha$ -particle induced signals). The electric  
129 field strength of both chambers,  $|\vec{E}|^{\text{H19}} = 240 \text{ V cm}^{-1}$   
130 and  $|\vec{E}|^{\text{PuFC}} = 300 \text{ V cm}^{-1}$ , was chosen to ensure fast  
131 signals and good timing properties.

132 The induced charges on the anodes of the PuFC were  
133 read out by in-house developed charge-sensitive pream-  
134 plifiers. Short rise times of approximately 80 ns and a  
135 signal length in the order of 400 ns reduce the pile-up

probability by a factor of 5 in comparison to the commonly used combination of a spectroscopic amplifier and a conventional preamplifier with  $\mu\text{s}$ -shaping time. Further details of the  $n\text{ELBE}$  fission chamber can be found in Ref. [24].

### C. Setup

H19 and PuFC were placed at a distance of 5.95 to 6.35 m with respect to the photo-neutron source and a distance of 10 cm between each other. The neutron beam diameter in this region is between 52 and 56 mm and, therefore, always smaller than the fission targets. The beam profile was measured at different points along the neutron beam axis by using horizontally and vertically scanning plastic scintillators and linearly interpolated to the region of interest (see Ref. [18]).

A sketch of the whole experimental setup is shown in Fig. 1. With the beam parameters chosen, the average neutron-induced fission rate of the H19 was about  $31\text{ s}^{-1}$ . The respective photo-fission rate was the nearly the same. For the PuFC, the neutron-induced fission rate was  $5\text{ s}^{-1}$ .

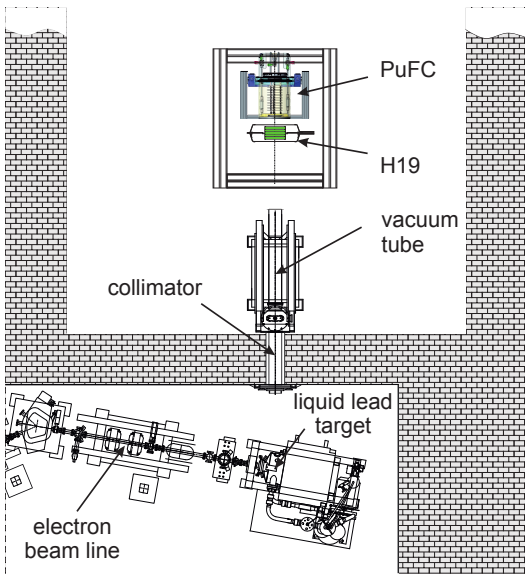


FIG. 1. Experimental setup. The ELBE electron beam comes from the lower left side and is guided to the photo-neutron source. A fraction of the isotropically emitted neutrons passes a collimator and enters the low-scattering experimental area. The incident neutron flux was measured with the  $^{235}\text{U}$  fission chamber H19. Fast neutron-induced fission events of  $^{242}\text{Pu}$  were recorded with the fission chamber PuFC. Picture not to scale.

### D. Data acquisition

The timing and energy information of both fission chambers was registered in list mode by the MBS data

acquisition software developed at GSI, Darmstadt [25]. A scheme of the VME-based data acquisition electronics is shown in Fig. 2.

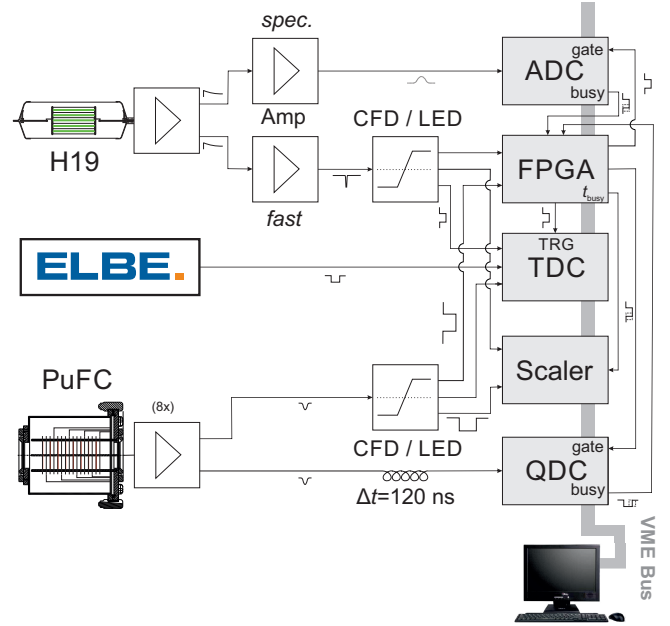


FIG. 2. Scheme of the electronic setup and the data acquisition system. The output signals of the charge-sensitive (ns-) preamplifiers are split to determine the timing and the collected charge. Pulse heights of the H19 signals are acquired with an ADC after getting shaped by a spectroscopic amplifier, whereas the charge of the eight PuFC channels (only one is shown here) is determined by a QDC. The production of a fast trigger makes the use of a timing-filter-amplifier in the timing branch of the H19 necessary. The second output signal is converted to a logical signal by an in-house developed discriminator (CFD/LED). The logical signals are used to determine the timing in a time-to-digital converter (TDC) and to produce a trigger for the data acquisition in an FPGA.

The signals from the 10 deposits of the H19 fission chamber were summed, amplified by one charge-sensitive preamplifier and afterwards measured by a conventional spectroscopic amplifier (Ortec 671) in the energy branch and by a timing-filter-amplifier (Ortec 474) in the timing branch. The signals of the eight  $^{242}\text{Pu}$  deposits were registered separately with the fast charge-sensitive preamplifiers mentioned in Sec. II B, to reduce possible pile-up of  $\alpha$ -radioactivity of the  $^{242}\text{Pu}$  even further.

The short signal length of the ns-preamplifier allows a charge-to-digital converter (QDC, CAEN V965A) to be used. The energy information of the H19 was determined by a peak-sensing analog-to-digital converter (ADC, CAEN V1785N).

The timing of the recorded signals was extracted by an in-house developed discriminator (CFD/LED), which combines a constant-fraction and a leading-edge discriminator. The neutron time-of-flight was measured relative to the ELBE radio frequency using a multi-event/multi-

hit time-to-digital converter (TDC, CAEN V1290A). The trigger for the whole data acquisition was a logical OR of all fission chamber channels generated by a multi-purpose board (FPGA, CAEN V1495). The leading-edge outputs of the discriminator as input for the FPGA prevents losing valid signals with slow rise-time, which otherwise will not be registered due to imperfect ARC-timing [26]. This was investigated to be especially important for small amplitude signals, mainly by  $\alpha$ -particles. The trigger thresholds and the delays of the CFD were chosen in a way, that the loss of fission fragments above the threshold was minimal, for both chambers integrally below 0.3%. Further details of the acquisition electronics can be found in Ref. [27].

### E. Analysis

The pulse-height information of the recorded list-mode data was used to separate time-independent background resulting due to the natural  $\alpha$ -decay of the target isotopes from the interesting fission events of interest. The charge spectra show the excellent quality of the  $^{242}\text{Pu}$  samples (cf. Fig. 3), which is expressed in a peak-to-valley ratio of 20 to 21 for all Pu-deposits.

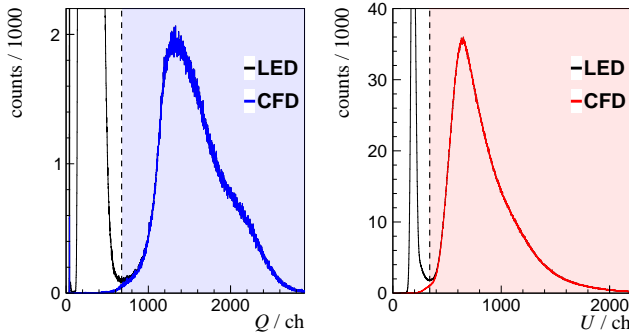


FIG. 3. Charge spectrum of channel #1 in the PuFC (left) and pulse height spectrum of the H19 (right). The leading-edge triggered QDC- and ADC values of the chambers are shown in black, the constant-fraction triggered ones in blue or red, respectively. The coloured areas indicate regions of pulse heights and charges related to fission fragments.

The time-of-flight spectra of each PuFC channel (e.g. channel #1, see Fig. 4(a)) and of the H19 (Fig. 4(b)) were calibrated with photo-fission events. The full width at half maximum of the photo-fission peak corresponds to the time resolution of the fission chambers. For the summed signal of all H19 deposits, this value is slightly higher (2.3 ns) than the single-readout PuFC (1.7 ns).

After subtraction of a constant spontaneous fission background, the  $^{242}\text{Pu}(n,f)$  fission rate  $\dot{N}_{\text{Pu},i}$  could be determined as a function of neutron kinetic energy shown in Fig. 4(a) on the right-hand side.

A consistent energy binning for all fission targets is chosen to combine the counts of individual channels of

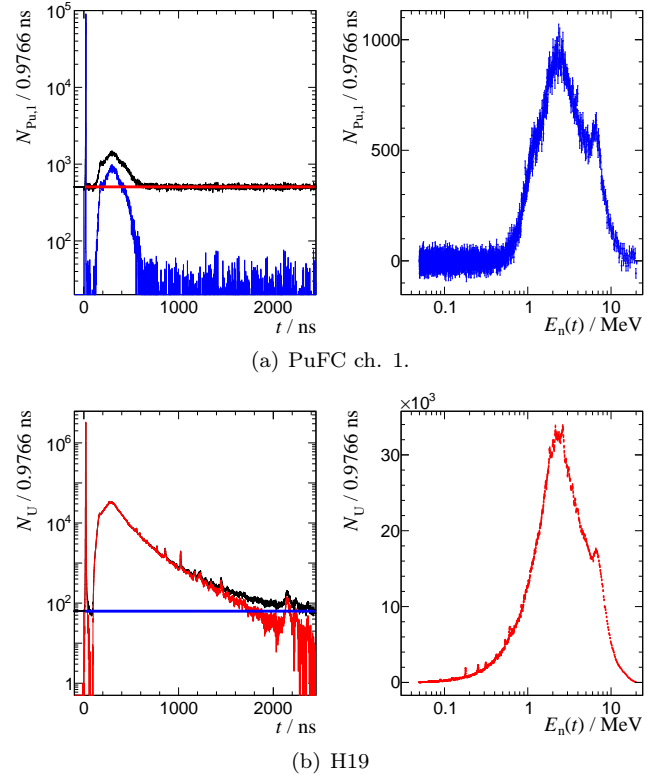


FIG. 4. Left: Detected time-of-flight spectrum  $N$  before (in black) and after (in blue for PuFC ch.1 and in red for H19) background subtraction. The horizontal red and blue lines indicate a constant extrapolation of the background induced by spontaneous fission events and room-return neutrons. Right: Background subtracted energy spectrum calculated using the time-of-flight spectrum shown on the left side.

the PuFC, which have slightly different flight paths [28]. After rebinning and background subtraction, the relative fission cross section is determined by:

$$\frac{\sigma_{\text{Pu}}}{\sigma_{\text{U}}} = K \frac{\sum_i C_{\text{Pu},i} \dot{N}_{\text{Pu},i}}{\langle C_{\text{U}} \rangle \dot{N}_{\text{U}}} \frac{1}{I}. \quad (1)$$

Eq. (1) is the ratio of the detected fission count rates  $\dot{N}$  of both fission chambers, taking into account a neutron scattering correction  $C$  between individual fission targets for the PuFC or  $\langle C_{\text{U}} \rangle$  averaged over all fission layers in the case of H19. This correction factor is discussed in detail in section II F. The constant factor  $K$  is the ratio of the effective total areal densities  $\varepsilon n$  of both fission chambers. Here,  $\varepsilon$  is the fission fragment detection efficiency which is in general difficult to determine. For the H19,  $\varepsilon_{\text{U}} n_{\text{U}} = 107.5(16) \cdot 10^{-17} \text{ cm}^{-2}$  was taken from Ref. [23], whereas for the PuFC,  $\varepsilon_{\text{Pu}} n_{\text{Pu}}$  was determined using the measured spontaneous fission rate of  $^{242}\text{Pu}$ . This method was already introduced by Weigmann *et al.* in Ref. [29], feasible because the total uncertainty of the spontaneous fission partial decay constant  $\lambda_{\text{SF}}$  is smaller than 2%

[30, 31]. Taking into account the recent measurement of Salvador-Castiñeira *et al.* from Ref. [32], the weighted average (weighting according to Ref. [31]) of all available data is  $\lambda_{\text{SF}} = 3.25(4) \cdot 10^{-19} \text{ s}^{-1}$ . An overview of all present data (expressed as  $\ln 2/\lambda_{\text{SF}}$ ) is given together with the evaluated values in Fig. 5.

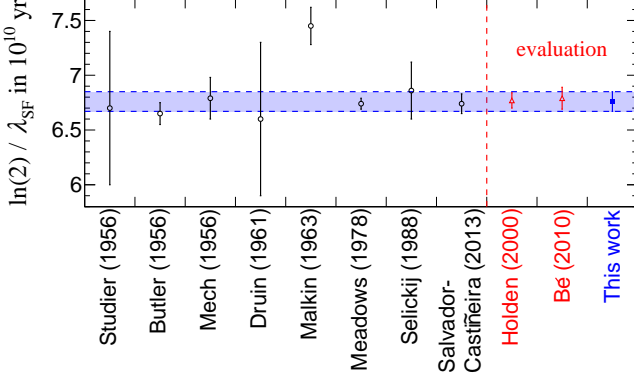


FIG. 5. Compilation of measured and evaluated partial half-lives for the spontaneous fission (SF) of  $^{242}\text{Pu}$ . The experimental data were taken from [30] and [32]. The re-evaluation of this data by Bé *et al.* [31] has a slightly higher uncertainty. In blue, the weighted average of all listed values is shown including the latest measurement of Salvador-Castiñeira *et al.* [32]. The blue shaded area marks the combined standard uncertainty of this value (1.3%).

As the area of the plutonium deposits  $A_{\text{Pu},i}$  is constant for all eight channels of the PuFC, the effective total areal density  $\varepsilon_{\text{Pu}} n_{\text{Pu}}$  is determined by:

$$\begin{aligned} \varepsilon_{\text{Pu}} n_{\text{Pu}} &= \sum_i \varepsilon_{\text{Pu},i} n_{\text{Pu},i} \\ &= \frac{\alpha}{A \lambda_{\text{SF}}} \sum_i \dot{N}_{(\text{SF}),i}. \end{aligned} \quad (2)$$

In Eq. (2) a small dead time correction ( $\approx 1\%$ ) of the DAQ is introduced denoted by  $\alpha$ . Using this relation, the normalization factor  $K$  can be written as follows:

$$K = \frac{\varepsilon_{\text{U}} n_{\text{U}}}{\varepsilon_{\text{Pu}} n_{\text{Pu}}} = A \frac{\lambda_{\text{SF}}}{\alpha} \frac{\varepsilon_{\text{U}} n_{\text{U}}}{\sum_i \dot{N}_{(\text{SF}),i}}. \quad (3)$$

Inserting  $K$  into Eq. (1) shows that the relative cross section is independent from the fission-fragment detection efficiency of the PuFC. This only holds for small neutron energies below 10 MeV because the higher the linear and angular momentum induced by the incident neutrons, the larger is the fission fragment anisotropy. This anisotropy lowers the detection efficiency. A model to calculate this effect was proposed by Carlson *et al.* in Ref. [33]. Due to the lack of experimental data for the fission fragment anisotropy and the barely known specific energy loss of fission fragments in the deposits, this inefficiency  $I$  is not an accurate value. An estimate based

on the angular correlation data of Simmons *et al.* [34], a GEF 2016.1.2 calculation [35] to determine the ratio of the target nuclei velocity to the average fission fragment velocity and a Geant 4.10.1 [36] transport calculation to determine the specific energy loss of the fission fragments in the deposit is shown in Fig. 6.

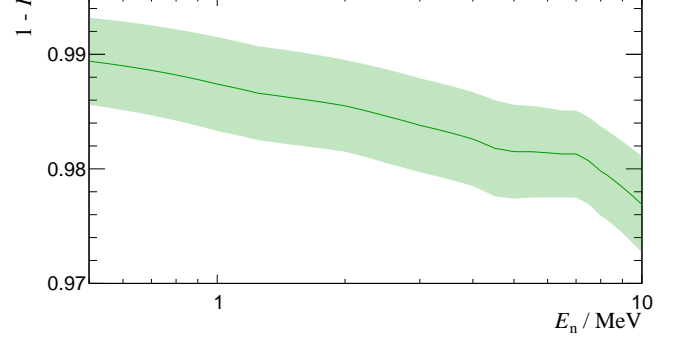


FIG. 6. Correction factor for the detection inefficiency  $I$  of fission fragments in the PuFC due to linear and angular momentum transfer according to the Carlson model [33].

## F. Neutron scattering corrections

Corrections for neutron scattering are an important issue in analyzing neutron time-of-flight experiments. Two major effects play an important role, the attenuation of the neutron beam in every passed material and the loss of the correlation between neutron kinetic energy and their corresponding time-of-flight.

The latter is important especially for inelastically scattered neutrons, because they lose a large amount of their kinetic energy within a single interaction. If such an event occurs close to a fission target, the kinetic energy of the scattered neutron determined from the measured time-of-flight will be much higher than the true kinetic energy and the cross section at high neutron energies will be overestimated. Particle transport calculations allow for correcting the influence of scattering as in these calculations both the true kinetic energy and the time-of-flight of the neutrons are accessible at once, which cannot be determined experimentally with the present setup. Such calculations have been performed using Geant 4.10.1 [36, 37], MCNP 6.1.1 [38] and Fluka 2011 [39, 40]. The geometry has been implemented identically in all three simulations with special attention to all materials close to the neutron beam. The outcome of all event-by-event calculations is a correlation matrix of the true kinetic energy  $E_n$  and the kinetic energy  $E_n(t)$  derived from their time-of-flight and the assumed undisturbed flight path. An example of such a correlation matrix for the last target in the beam (PuFC channel #1) is shown in Fig. 7.

Because scattering cross sections are energy-dependent, it is necessary to use a realistic input spectrum in



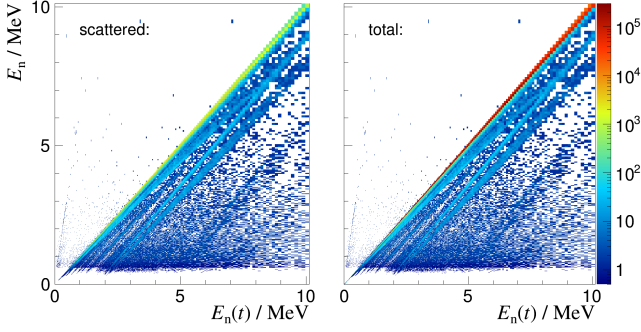


FIG. 7. Energy to time-of-flight-correlation of the last PuFC deposit in the neutron beam calculated using Geant 4.10.1. On the right-hand side, all neutrons passing the actinide target are shown, whereas on the left-hand side, only events are drawn, which have been scattered at least once. The bin content of each histogram was multiplied column-wise with the  $^{242}\text{Pu}$  fission cross section at the respective neutron energy  $E_n$  to be proportional to the fission rate. Structures off the diagonal are caused by elastic and inelastic scattering on the target backing (mostly  $^{28}\text{Si}$ ) and stainless steel windows of the fission chamber (mostly  $^{56}\text{Fe}$ ).

the simulations. The measured neutron fluence detected by the H19 was used for this purpose. The influence of neutron scattering within the H19 itself is negligible.

To correct the attenuation of the neutron beam, one can define a transmission factor

$$T_i(E_n(t)) = \frac{N_i(E_n = E_n(t))}{N_0(E_n)}, \quad (4)$$

which is the ratio of all counted neutrons  $N_i$  in the  $i$ -th actinide target, that have not been scattered on their way to the target (on the main diagonal on the right of Fig. 7), and the total number of neutrons  $N_0$  started from the neutron source. The average loss of neutrons between the first and last fission target is in the order of 15 %, which is a consequence of the thickness of the Si-backings and the 200  $\mu\text{m}$  stainless steel windows of the PuFC.

For the loss of the energy to time-of-flight correlation, a similar correction factor  $k_i$  is defined.

$$k_i(E_n(t)) = \frac{N_i(E_n = E_n(t), E_n(t))\sigma(E_n)}{\int N_i(E'_n, E_n(t))\sigma(E'_n)dE'_n} \quad (5)$$

Scattered neutrons could still contribute to fission, so that  $k_i$  is the ratio of the detected fission rate of unscattered neutrons and the total detected fission rate. Because the fission rate depends on the cross section, the correlation matrices have been multiplied column-wise with the evaluated fission cross section of  $^{242}\text{Pu}$  taken from ENDF/B-VIII.0. [41], which is for this particular reaction identical to its predecessor ENDF/B-VII.1 [13].

With Eq. (4) and Eq. (5), the neutron scattering correction factor  $C_i(E_n(t))$  is defined in the following way:

$$C_i = \frac{k_i}{T_i} \quad (6)$$

As only the sum of all H19 fission targets is available, the arithmetic mean  $\langle C_U \rangle$  was calculated to take the neutron scattering within this chamber into account. The average total correction factor is in the order of 9 % and shown for all three simulations in Fig. 8. While Geant 4 and MCNP 6 provide identical results within their statistical fluctuations, the Fluka 2011 results show a negligible shift towards a higher correction factor.

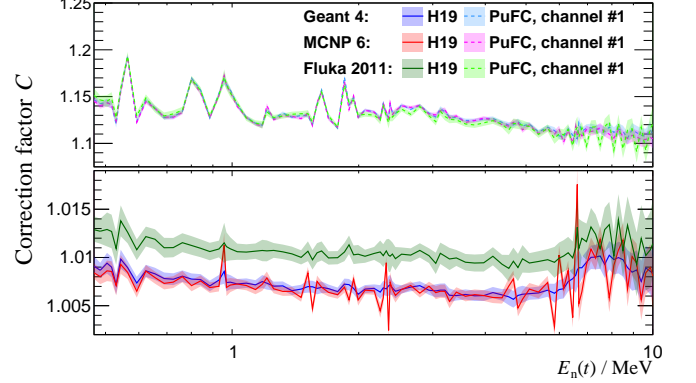


FIG. 8. Correction factor  $C$  for neutron scattering derived from Geant 4 (blue), MCNP 6 (red) and Fluka 2011 (green). This plot shows the maximum effect by comparing the first target of the H19 (lower panel) with the last target (PuFC, channel #1, upper panel) in the neutron beam. The confidence intervals shown here correspond to the  $1\sigma$  statistical uncertainty.

The correction procedure was verified by evaluating the ratio of neutron-induced and spontaneous fission rate of the PuFC. Whereas the spontaneous fission is completely independent from any scattering, the neutron-induced is not. The ratio shows an exponential decrease along the plutonium chamber (red line in Fig. 9) and becomes constant after applying the neutron scattering correction (blue line in Fig. 9).

### III. RESULTS AND DISCUSSION

With the scattering corrections in Sec. II F and the normalization constants listed in Tab. III, we are now able to calculate the relative fission cross section according to Eq. (1). The result is shown in Fig. 10 and compared to the measurements of Tovesson *et al.* [10], Staples *et al.* [42] and Weigmann *et al.* [29].

Because only the relative data of Staples *et al.* were included in the EXFOR database [43], the absolute cross section of the other two has been divided by their reported reference cross section to fit into this plot.

To compare our measurement with other recent data sets as well, the absolute cross section was determined

TABLE III. Normalization constants

$\lambda_{\text{SF}}$	$= 3.25(4) \cdot 10^{-19} \text{ s}^{-1}$	SF partial decay constant, cf. Fig. 5
$A$	$= 43.0(5) \text{ cm}^2$	actinide area, from deposition cell
$\varepsilon_{\text{U}}$	$= 0.945(14)$	fission fragment detection efficiency H19, Ref. [23]
$n_{\text{U}}$	$= 113.8(3) \cdot 10^{17} \text{ cm}^{-2}$	atomic areal density H19, Ref. [23]
$\alpha \sum_i \varepsilon_{\text{Pu},i} \dot{N}_{(\text{SF}),i}$	$= 29.688(4) \text{ s}^{-1}$	measured SF-rate
$K$	$= 5.04(12)$	total normalization

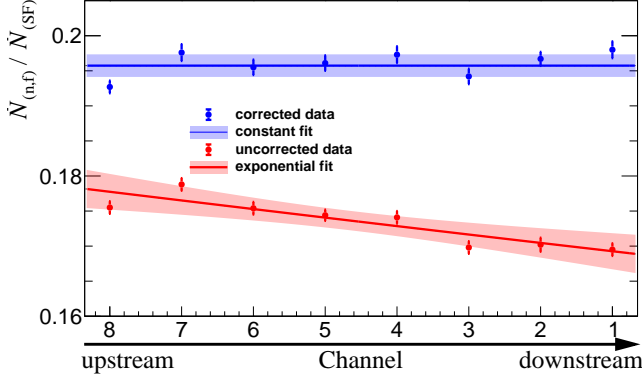


FIG. 9. Ratio of neutron-induced and spontaneous fission rate without (red) and with (blue) correction for neutron scattering. Without the correction, the fraction of the neutron-induced fission rate drops exponentially between the fission chamber channels, whereas the spontaneous fission rate stays constant. Note that channel #8 corresponds to the deposit closest to the neutron source while channel 1 is the farthest from it, thus having the largest absorption correction.

ent target-beam combinations were used. It seems that the systematic effects in these experiment were taken into account in a realistic way resulting in a consistent weighted average with less than 2 % uncertainty.

TABLE IV. Average deviations  $\Delta = \frac{\sigma_{\text{EXFOR}}}{\sigma_{n\text{ELBE}}} - 1$  of the measured  $^{242}\text{Pu}(n,f)$  cross sections with respect to selected EXFOR data in the energy range of 0.5-10 MeV. The listed reduced chi square ( $\chi^2/n$ ) and the  $p$ -value are a measure for the agreement in shape.

Measurement	$\Delta$ in %	$n\text{ELBE}$ $\chi^2/n$	$p$ in %
Weigmann <i>et al.</i> , 1984	3.82(16)	229.76 / 161 = 1.43	0
Staples <i>et al.</i> , 1998	-2.59(20)	164.68 / 100 = 1.65	0
Tovesson <i>et al.</i> , 2009	0.67(16)	178.69 / 259 = 0.69	100
Salvador-Castiñeira <i>et al.</i> , 2015	0.7(3)	179.46 / 23 = 7.80	0
Matei <i>et al.</i> , 2017	4.6(8)	5.43 / 4 = 1.36	25
Marini <i>et al.</i> , 2017	2(1)	8.19 / 3 = 2.73	4

using the  $^{235}\text{U}$ -IAEA Neutron Cross Section Standard from Ref. [44]. This is shown in Fig. 11. All data shown in this plot were re-normalized with the same standard.

One can see that there is a good overall agreement of the  $n\text{ELBE}$  data compared to the other selected data sets presented here. While the ratio of the  $n\text{ELBE}$  and the Tovesson *et al.* and Salvador-Castiñeira *et al.* data is about 0.99, larger discrepancies to the Matei *et al.* and Weigmann *et al.* data were observed especially in the plateau region between 1.2 - 5 MeV. This is of special interest, because the current European evaluation JEFF-3.3 [45] relies mainly on the latter one [29]. A comparison of shape and scale parameters of the other experimental data sets with respect to the  $n\text{ELBE}$  data is listed in Tab. IV. The average deviations with respect to ENDF/B-VIII.0 (shown in Fig. 12) are presented in Fig. 13, where the residuals of the EXFOR data are approximated by a constant. All experiments shown are on average in good agreement within their total uncertainties. The experimental data of [8, 10, 12, 42] and this work on the average tend to be 4 % lower than ENDF/B-VIII.0. In these experiments different neutron sources (spallation, photo-neutron and quasi-monoenergetic neutrons) with different reference reactions as well as differ-

## A. Uncertainties

Table V gives an overview of the respective contributions to the statistical and systematic uncertainties.

For an energy range of 0.87 to 8.5 MeV the statistical uncertainty of the background-corrected counts within a 2 ns time-of-flight binning is below 3 %. The highest significance is reached in the plateau region, whereas the largest uncertainties are in the threshold and second-chance fission region, where the neutron fluence of  $n\text{ELBE}$  is too low to achieve better statistics within the available measuring time of 80 h.

The systematic contributions from the reference cross section and the scattering corrections described in section IIF are always below 1 % over the whole energy range. The effect of fission fragment detection inefficiency caused by the fragment anisotropy at high neutron energies (discussed in section IIE) increases with increasing neutron energy and is 1.6 % on average for the included energy range. The largest contribution to the combined averaged systematic uncertainty of 2.9 %, though, results from the uncertainty on the target area ( $\sigma_A/A \approx 1.1$  %). Although radiographic images show a



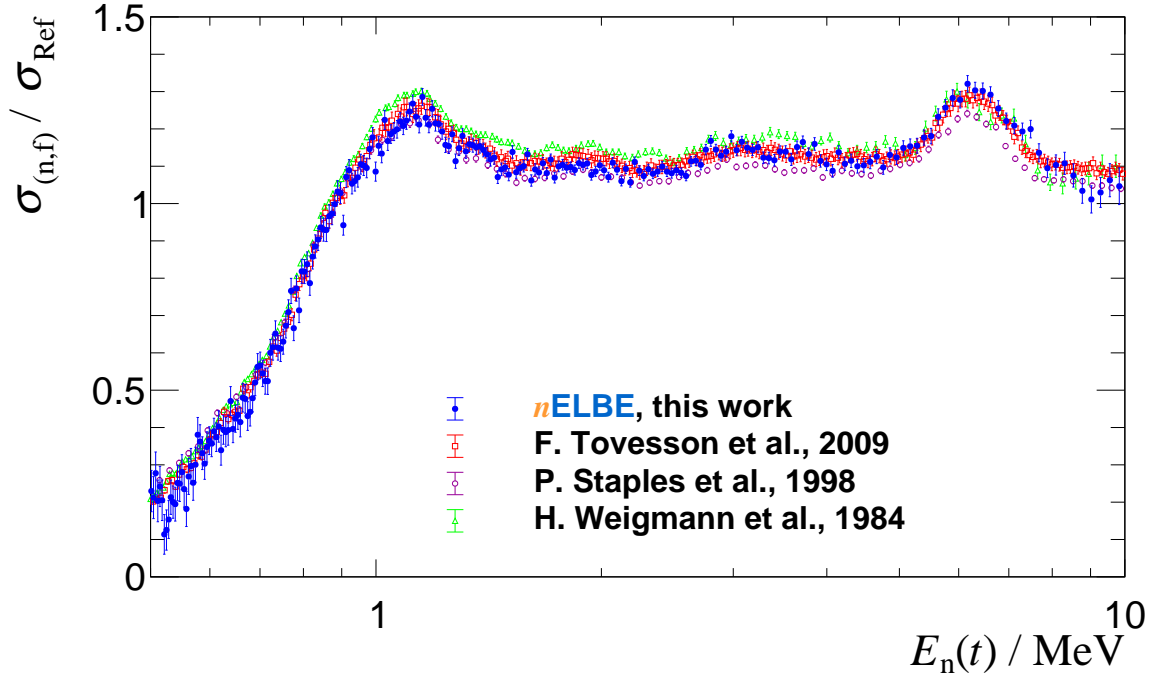


FIG. 10. Neutron-induced fission cross section of  $^{242}\text{Pu}$  relative to the one of  $^{235}\text{U}$ . The  $n\text{ELBE}$  data are shown in blue together with selected EXFOR-data of Tovesson *et al.* [10], Staples *et al.* [42] and Weigmann *et al.* [29]. Within their statistical uncertainties, there is a good agreement of the presented data set with the data of Tovesson. Small deviations from the Weigmann and Staples data are clearly visible.

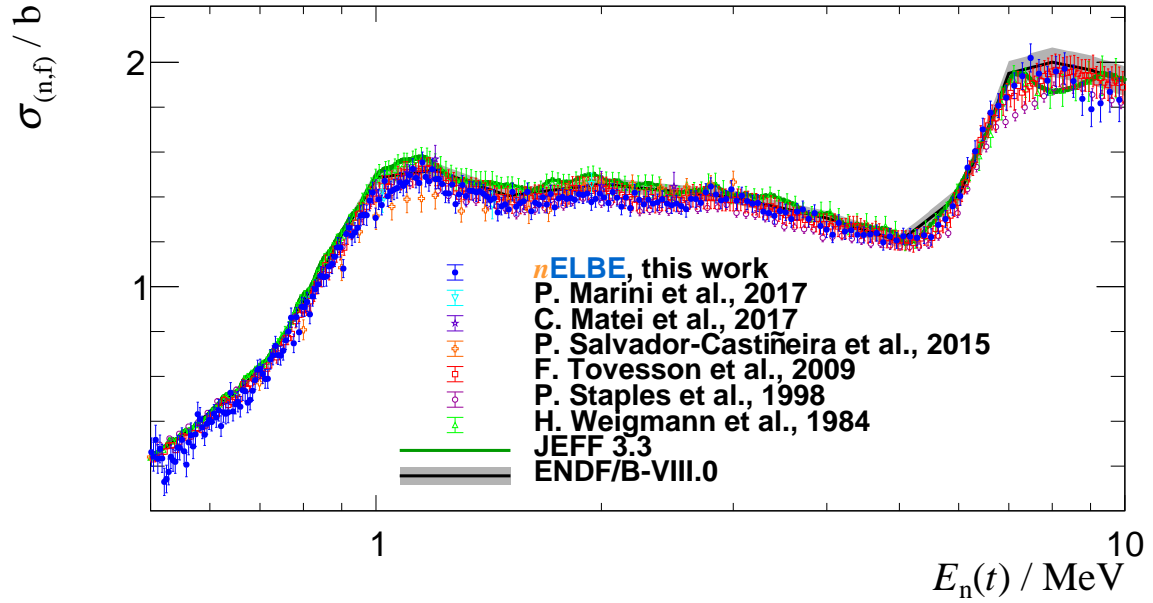


FIG. 11. Neutron-induced fission cross section of  $^{242}\text{Pu}$ . The  $n\text{ELBE}$  data are shown in blue together with selected EXFOR-data of Tovesson *et al.* [10], Staples *et al.* [42], Weigmann *et al.* [29] and Salvador-Castiñeira *et al.* [8]. Within their total uncertainties, there is a good agreement of the presented data set with the data of Tovesson. Small deviations from the Weigmann data and the measurement of Salvador-Castiñeira are clearly visible.

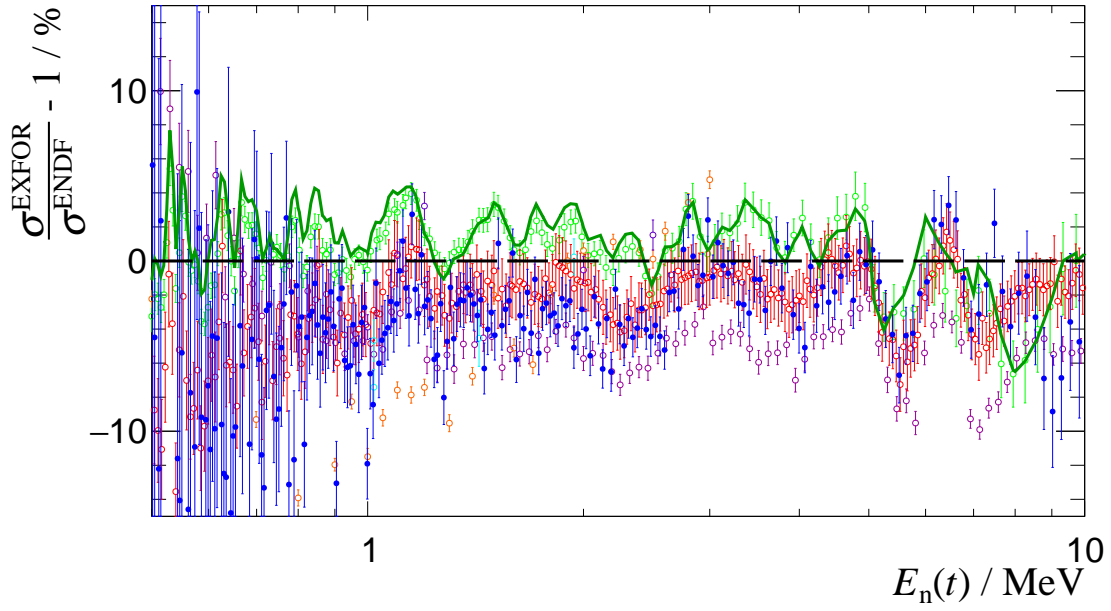


FIG. 12. Residuals of the discussed data sets shown in Fig. 11 with respect to the ENDF/B-VIII.0 evaluation. The error bars plotted here only represent the statistical uncertainty of the measurements. The used color code is identical to that in Fig. 11

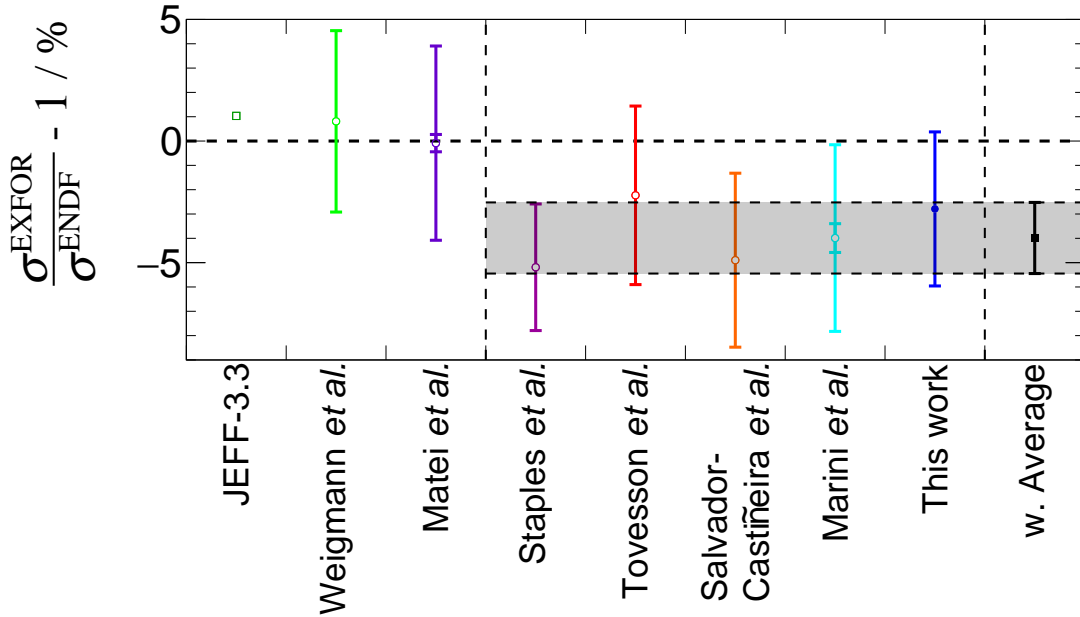


FIG. 13. Average deviations of JEFF-3.3 and selected EXFOR data sets with respect to ENDF/B-VIII.0. The weighted average has been determined by fitting a constant to the residuals shown in Fig. 12. Error bars indicating both, the statistical and the total uncertainty, are drawn for each data point. With the exception of the Weigmann *et al.* and Matei *et al.* data, all recent measurements tend on average to 4.1(15)% smaller cross-sections compared to ENDF/B-VIII.0.

TABLE V. Contributions to the  $1\sigma$ -uncertainty of the determined cross section for neutron energies between 0.5-10 MeV and a time-of-flight binning of 2 ns.

Contribution	$\Delta x/x$ in %		
	min	max	mean
statistical			
counting statistics	1.2	47.4	4.9
scattering correction $C^a$	0.17	0.93	0.21
systematic			
normalization $K$			2.3
reference cross-section $\sigma_{\text{Ref}}$	0.6	0.8	0.7
scattering correction $C^b$	0.17	0.93	0.21
Inefficiency $I$ , cf. Fig. 6	0.38	0.43	0.41
<b>combined:</b>			<b>2.9</b>

<sup>a</sup> The uncertainty given here only reflects the counting statistics of the simulation

<sup>b</sup> From the propagated uncertainty of the underlying total cross sections

very homogeneous activity distribution along the whole surface (cf. Fig. 4.1.4. and 4.1.5 in Ref. [27]), the distribution at the target edges is not assessable. A conservative assumption was taken here to consider edge effects in the order of 0.4 mm with respect to the target diameter.

#### B. Comparison with state of the art nuclear model codes

Recent nuclear model calculations show substantial deviations in comparison to all experimental neutron-induced fission cross section data of  $^{242}\text{Pu}$ . This is exemplarily demonstrated in Fig. 14.

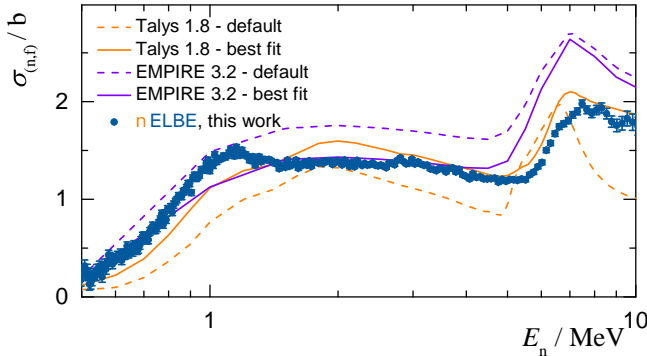


FIG. 14. Comparison of the  $n\text{ELBE}$  data with nuclear model calculations from Talys 1.8 and EMPIRE 3.2.

Here the  $n\text{ELBE}$  data are shown together with results from calculations performed with the nuclear model code Talys 1.8 [46] and with EMPIRE 3.2 [47, 48]. For both

one calculation was performed with the default settings of the code and one with an improved set of parameters. For EMPIRE, the fission barrier heights and widths have been adjusted to fit with the data. The same was also done in Talys, but here widths, heights and additional parameters of the “Adjusted Input-Parameters” of TENDL 2017 [49] were used.

The results demonstrate that nuclear fission is one of the most complex nuclear reactions and that current nuclear model codes cannot yet predict fission cross sections with the accuracy required for some technological applications.

#### IV. CONCLUSIONS

The fast neutron-induced fission cross section of  $^{242}\text{Pu}$  has been measured in the range of 0.5-10 MeV at  $n\text{ELBE}$ . It is in good agreement to recent experimental data from different neutron facilities. The  $n\text{ELBE}$  data shows a smaller cross section compared to recently evaluated data. In the plateau region (1.3 to 5.0 MeV), the agreement with the Staples *et al.* ( $\Delta = -2.51(24)\%$ ,  $\chi^2/n = 1.12$ ) and Tovesson *et al.* ( $\Delta = 0.83(20)\%$ ,  $\chi^2/n = 0.54$ ) data is excellent. We encountered deviations from the data of Weigmann *et al.* ( $\Delta = 3.81(19)\%$ ,  $\chi^2/n = 1.16$ ), which the JEFF-3.3 evaluation is mainly based on. At the plateau, where  $n\text{ELBE}$  has the largest neutron fluence, we achieved a statistical uncertainty of 1.1 %. The systematic uncertainty is dominated by edge effects of the actinide targets and is in the order of 2.9 % on average over the measured energy range.

It has been shown that neutron scattering corrections are crucial in analyzing neutron time-of-flight experiments. For the present data, the average correction was around 9 %.

In comparison to state of the art nuclear model codes like Talys 1.8 and EMPIRE 3.2, deviations of about 20 % to 30 % from all experiments are observed. This might be indicative of the predictive power of such codes on an absolute scale for neutron-induced fission cross sections of the minor actinides. Precise measurements remain the basis for nuclear data evaluation of fission cross sections.

#### ACKNOWLEDGMENTS

We thank Manfred Sobiella and Klaus Heidel for the support in the construction of the fission chamber and the preamplifiers. We also thank Andreas Hartmann for the continuous support in the preparation of our experiments. Thanks also go to the ELBE accelerator crew, who take care of delivering a stable and reliable beam. This work was supported by the German Federal Ministry of Education and Research under contract no. 02NUK13A and by the European Commission within the 7<sup>th</sup> framework programme Fission-2013-CHANDA (project number 605203).

- [1] The Generation IV International Forum (GIF), *Technology Roadmap Update for Generation IV Nuclear Energy Systems*, Roadmap (Nuclear Energy Agency (NEA) and Organisation for Economic Co-Operation and Development (OECD), 2014).
- [2] Y. Akovali, Nucl. Data Sheets **96**, 177 (2002).
- [3] A. Schwenk-Ferrero, Science and Technology of Nuclear Installations **2013**, 1 (2013).
- [4] WPEC, *Uncertainty and Target Accuracy Assessment for Innovative Systems Using Recent Covariance Data Evaluations*, Tech. Rep. (Working Party on International Evaluation Co-Operation, OECD / NEA, 2008).
- [5] Working Party on International Evaluation Co-Operation, OECD / NEA, “The High Priority Request List for Nuclear Data (HPRL),” (2011).
- [6] IAEA, “Inden: International nuclear data evaluation network,” (2018).
- [7] A. Butler, Phys. Rev. **117**, 1305 (1960).
- [8] P. Salvador-Castiñeira, T. Brys, R. Eykens, F.-J. Hambach, A. Göök, A. Moens, S. Oberstedt, G. Sibbens, D. Vanleeuw, M. Vidali, and C. Pretel, Phys. Rev. C **92**, 044606 (2015).
- [9] I. Alkharov, E. Ganza, L. Drapchinskij, V. Dushin, S. Kovalenko, O. Kostochkin, K. Petrzhak, A. Fomichev, V. Shpakov, R. Arlt, W. Wagner, M. Josch, G. Musiol, H.-G. Ortlepp, and G. Pausch, in *Proc. of the 3<sup>rd</sup> All-Union Conference on the Neutron Radiation Metrology at Reactors and Accelerators, Moscow*, Vol. 2 (1983) p. 201.
- [10] F. Tovesson, T. Hill, M. Mocko, J. Baker, and C. McGrath, Phys. Rev. C **79**, 014613 (2009).
- [11] C. Matei, F. Belloni, J. Heyse, A. J. M. Plompen, and D. J. Thomas, Phys. Rev. C **95**, 024606 (2017).
- [12] P. Marini, L. Mathieu, M. Aiche, G. Belier, S. Czajkowski, Q. Ducasse, B. Jurado, G. Kessedjian, J. Mataranz, A. Plompen, P. Salvador-Castiñeira, J. Taieb, and I. Tsekhanovich, Phys. Rev. C **96**, 054604 (2017).
- [13] M. Chadwick, M. Herman, P. Obložinský, M. Dunn, Y. Danon, A. Kahler, D. Smith, B. Pritychenko, G. Arbanas, R. Arcilla, R. Brewer, D. Brown, R. Capote, A. Carlson, Y. Cho, H. Derrien, K. Guber, G. Hale, S. Hoblit, S. Holloway, T. Johnson, T. Kawano, B. Kiedrowski, H. Kim, S. Kunieda, N. Larson, L. Leal, J. Lestone, R. Little, E. McCutchan, R. MacFarlane, M. MacInnes, C. Mattoon, R. McKnight, S. Mughabghab, G. Nobre, G. Palmiotti, A. Palumbo, M. Pigni, V. Pronyaev, R. Sayer, A. Sonzogni, N. Summers, P. Talou, I. Thompson, A. Trkov, R. Vogt, S. van der Marck, A. Wallner, M. White, D. Wiarda, and P. Young, Nucl. Data Sheets **112**, 2887 (2011).
- [14] A. Junghans, R. Beyer, E. Grosse, R. Hannaske, T. Kögler, R. Massarczyk, R. Schwengner, and A. Wagner, Eur. Phys. J.: Web of Conferences **93**, 02015 (2015).
- [15] IAEA, “International Evaluation of Neutron Cross-Section Standards,” (2007), ISBN 92-0-100807-4.
- [16] E. Altstadt, C. Beckert, H. Freiesleben, V. Galindo, E. Grosse, A. Junghans, J. Klug, B. Naumann, S. Schneider, R. Schlenk, A. Wagner, and F.-P. Weiss, Ann. Nucl. Energy **34**, 36 (2007).
- [17] J. Klug, E. Altstadt, C. Beckert, R. Beyer, H. Freiesleben, V. Galindo, E. Grosse, A. Junghans, D. Légrády, B. Naumann, K. Noack, G. Rusev, K. Schilling, R. Schlenk, S. Schneider, A. Wagner, and F.-P. Weiss, Nucl. Instrum. Meth. A **577**, 641 (2007).
- [18] R. Beyer, E. Birgersson, Z. Elekes, A. Ferrari, E. Grosse, R. Hannaske, A. Junghans, T. Kögler, R. Massarczyk, A. Matić, R. Nolte, R. Schwengner, and A. Wagner, Nucl. Instrum. Meth. A **723**, 151 (2013).
- [19] T. Kögler, R. Beyer, R. Hannaske, A. Junghans, R. Massarczyk, and A. Wagner, Phys. Proc. **47**, 178 (2013).
- [20] T. Kögler, R. Beyer, A. R. Junghans, R. Massarczyk, R. Schwengner, and A. Wagner, Phys. Proc. **64**, 150 (2015).
- [21] A. Vascon, J. Runke, N. Trautmann, B. Cremer, K. Eberhardt, and C. Düllmann, Appl. Radiat. Isot. **95**, 36 (2015).
- [22] D. B. Gayther, Metrologia **27**, 221 (1990).
- [23] R. Nolte, M. S. Allie, F. D. Brooks, A. Buffler, V. Dangendorf, J. P. Meulders, H. Schuhmacher, F. D. Smit, and M. Weierganz, Nucl. Sci. Eng. **156**, 197 (2007).
- [24] T. Kögler, R. Beyer, K. Eberhardt, K. Heide, A. Hartmann, A. R. Junghans, S. E. Müller, R. Nolte, M. Sobbiella, A. Vascon, and A. Wagner, Nucl. Instrum. Meth. A (2018 (in preparation)).
- [25] H. G. Essel and N. Kurz, *GSI Multi-Branch System - Reference Manual*, GSI, Gesellschaft für Schwerionenforschung mbH, Planckstraße 1, D-64291 Darmstadt, Germany, 5th ed. (2010).
- [26] Z. Cho and R. Chase, Nucl. Instrum. Meth. **98**, 335 (1972).
- [27] T. Kögler, *Bestimmung des Neutronen-induzierten Spaltquerschnitts von  $^{242}\text{Pu}$* , Dissertation, Technische Universität Dresden (2016).
- [28] T. Kögler, R. Beyer, M. Dietz, A. R. Junghans, C. Lorenz, S. E. Müller, T. P. Reinhardt, K. Schmidt, R. Schwengner, M. P. Takacs, and A. Wagner, *ND 2016 International Conference on Nuclear Data for Science and Technology*, Eur. Phys. J.: Web of Conferences **146**, 11023 (2017).
- [29] H. Weigmann, J. Wartena, and C. Bürkholz, Nucl. Phys. A **438**, 333 (1985).
- [30] N. E. Holden and D. C. Hoffman, Pure Appl. Chem. **72**, 1525 (2000).
- [31] M.-M. Bé, V. Chisté, C. Dulieu, X. Mougeot, E. Browne, V. Chechev, N. Kuzmenko, F. Kondev, A. Luca, M. Galán, A. Nichols, A. Arinc, and X. Huang, *Table of Radionuclides*, Monographie BIPM-5, Vol. 5 (Bureau International des Poids et Mesures, Pavillon de Breteuil, F-92310 Sèvres, France, 2010).
- [32] P. Salvador-Castiñeira, T. Brys, R. Eykens, F.-J. Hambach, A. Moens, S. Oberstedt, G. Sibbens, D. Vanleeuw, M. Vidali, and C. Pretel, Phys. Rev. C **88**, 064611 (2013).
- [33] G. W. Carlson, Nucl. Instrum. Meth. **119**, 97 (1974).
- [34] J. E. Simmons, R. B. Perkins, and R. L. Henkel, Phys. Rev. **137**, B809 (1965).
- [35] K.-H. Schmidt, B. Jurado, and C. Amouroux, *General Description of Fission Observables – GEF Model*, JEFF Report 24 (Nuclear Energy Agency (NEA) and Organisation for Economic Co-Operation and Development (OECD), Gradignan, France, 2014).
- [36] J. Allison, S. Agostinelli, K. Amako, J. Apostolakis,

- H. Araujo, P. Arce, M. Asai, D. Axen, S. Banerjee, G. Barrand, F. Behner, L. Bellagamba, J. Boudreau, L. Broglia, A. Brunengo, H. Burkhardt, S. Chauvie, J. Chuma, R. Chytráček, G. Cooperman, G. Cosmo, P. Degtyarenko, A. Dell'Acqua, G. Depaola, D. Dietrich, R. Enami, A. Feliciello, C. Ferguson, H. Fesefeldt, G. Folger, F. Foppiano, A. Forti, S. Garelli, S. Giani, R. Giannitrapani, D. Gibin, J. G. Cadenas, I. González, G. G. Abril, G. Greeniaus, W. Greiner, V. Grichine, A. Grossheim, S. Guatelli, P. Gumplinger, R. Hamatsu, K. Hashimoto, H. Hasui, A. Heikkinen, A. Howard, V. Ivanchenko, A. Johnson, F. Jones, J. Kallenbach, N. Kanaya, M. Kawabata, Y. Kawabata, M. Kawaguti, S. Kelner, P. Kent, A. Kimura, T. Kodama, R. Kokoulin, M. Kossov, H. Kurashige, E. Lamanna, T. Lampén, V. Lara, V. Lefebvre, F. Lei, M. Liendl, W. Lockman, F. Longo, S. Magni, M. Maire, E. Medernach, K. Minamimoto, P. M. de Freitas, Y. Morita, K. Murakami, M. Nagamatsu, R. Nartallo, P. Nieminen, T. Nishimura, K. Ohtsubo, M. Okamura, S. O'Neale, Y. Oohata, K. Paech, J. Perl, A. Pfeiffer, M. Pia, F. Ranjard, A. Rybin, S. Sadilov, E. D. Salvo, G. Santin, T. Sasaki, N. Savvas, Y. Sawada, S. Scherer, S. Sei, V. Sirotenko, D. Smith, N. Starkov, H. Stoecker, J. Sulkimo, M. Takahata, S. Tanaka, E. Tcherniaev, E. S. Tehrani, M. Tropeano, P. Truscott, H. Uno, L. Urban, P. Urban, M. Verderi, A. Walkden, W. Wander, H. Weber, J. Wellisch, T. Wenaus, D. Williams, D. Wright, T. Yamada, H. Yoshida, and D. Zschiesche, *Nucl. Instrum. Meth. A* **506**, 250 (2003).
- [37] J. Allison, K. Amako, J. Apostolakis, P. Arce, M. Asai, T. Aso, E. Bagli, A. Bagulya, S. Banerjee, G. Barrand, B. Beck, A. Bogdanov, D. Brandt, J. Brown, H. Burkhardt, P. Canal, D. Cano-Ott, S. Chauvie, K. Cho, G. Cirrone, G. Cooperman, M. Cortés-Giraldo, G. Cosmo, G. Cuttone, G. Depaola, L. Desorgher, X. Dong, A. Dotti, V. Elvira, G. Folger, Z. Francis, A. Galoyan, L. Garnier, M. Gayer, K. Genser, V. Grichine, S. Guatelli, P. Guèye, P. Gumplinger, A. Howard, I. Hrivnáčová, S. Hwang, S. Incerti, A. Ivanchenko, V. Ivanchenko, F. Jones, S. Jun, P. Kaitaniemi, N. Karakatsanis, M. Karamitros, M. Kelsey, A. Kimura, T. Koi, H. Kurashige, A. Lechner, S. Lee, F. Longo, M. Maire, D. Mancusi, A. Mantero, E. Mendoza, B. Morgan, K. Murakami, T. Nikitina, L. Pandola, P. Paprocki, J. Perl, I. Petrović, M. Pia, W. Pokorski, J. Quesada, M. Raine, M. Reis, A. Ribon, A. R. Fira, F. Romano, G. Russo, G. Santin, T. Sasaki, D. Sawkey, J. Shin, I. Strakovsky, A. Taborda, S. Tanaka, B. Tomé, T. Toshito, H. Tran, P. Truscott, L. Urban, V. Uzhinsky, J. Verbeke, M. Verderi, B. Wendt, H. Wenzel, D. Wright, D. Wright, T. Yamashita, J. Yarba, and H. Yoshida, *Nucl. Instrum. Meth. A* **835**, 186 (2016).
- [38] T. Goorley, *MCNP 6.1.1 - Beta Release Notes*, techreport (Los Alamos National Laboratory, 2014).
- [39] A. Ferrari, P. R. Sala, A. Fasso, and J. Ranft, in *CERN 2005-10*, Vol. 10 (CERN European Organization for Nuclear Research, 2005).
- [40] T. Böhlen, F. Cerutti, M. Chin, A. Fassò, A. Ferrari, P. Ortega, A. Mairani, P. Sala, G. Smirnov, and V. Vlachoudis, *Nucl. Data Sheets* **120**, 211 (2014).
- [41] D. Brown, M. Chadwick, R. Capote, A. Kahler, A. Trkov, M. Herman, A. Sonzogni, Y. Danon, A. Carlson, M. Dunn, D. Smith, G. Hale, G. Arbanas, R. Arcilla, C. Bates, B. Beck, B. Becker, F. Brown, R. Casperson, J. Conlin, D. Cullen, M.-A. Descalle, R. Firestone, T. Gaines, K. Guber, A. Hawari, J. Holmes, T. Johnson, T. Kawano, B. Kiedrowski, A. Koning, S. Kopecky, L. Leal, J. Lestone, C. Lubitz, J. M. Damián, C. Mattoon, E. McCutchan, S. Mughabghab, P. Navrátil, D. Neudecker, G. Nobre, G. Noguere, M. Paris, M. Pigni, A. Plompen, B. Pritychenko, V. Pronyaev, D. Roubtsov, D. Rochman, P. Romano, P. Schillebeeckx, S. Simakov, M. Sin, I. Sirakov, B. Sleaford, V. Sobes, E. Soukhovitskii, I. Stetcu, P. Talou, I. Thompson, S. van der Marck, L. Welser-Sherrill, D. Wiarda, M. White, J. Wormald, R. Wright, M. Zerkle, G. Zerovnik, and Y. Zhu, *Nucl. Data Sheets* **148**, 1 (2018).
- [42] P. Staples and K. Morley, *Nucl. Sci. Eng.* **129**, 149 (1998).
- [43] N. Otuka, E. Dupont, V. Semkova, B. Pritychenko, A. Blokhin, M. Aikawa, S. Babykina, M. Bossant, G. Chen, S. Dunaeva, R. Forrest, T. Fukahori, N. Furutachi, S. Ganesan, Z. Ge, O. Gritzay, M. Herman, S. Hlavac, K. Kato, B. Lalremruata, Y. Lee, A. Makinaga, K. Matsumoto, M. Mikhaylyukova, G. Pikulina, V. Pronyaev, A. Saxena, O. Schwerer, S. Simakov, N. Soppera, R. Suzuki, S. Takács, X. Tao, S. Taova, F. Tárkányi, V. Varlamov, J. Wang, S. Yang, V. Zerkina, and Y. Zhuang, *Nucl. Data Sheets* **120**, 272 (2014).
- [44] S. Badikov, C. Zhenpeng, A. Carlson, E. Gai, G. Hale, F.-J. Hambsch, H. Hofmann, T. Kawano, N. Larson, V. Pronyaev, D. Smith, S.-Y. Oh, S. Tagesen, and H. Vonach, *International Evaluation of Neutron Cross-Section Standards*, Technical Report 07-00494 (International Atomic Energy Agency, Wagramer Straße 5, P.O. Box 100, 1400 Vienna, Austria, 2007).
- [45] OECD and NEA, "The joint evaluated fission and fusion file (jeff) - version 3.3," (2018).
- [46] A. Koning and D. Rochman, *Nucl. Data Sheets* **113**, 2841 (2012).
- [47] M. Herman, R. Capote, B. Carlson, P. Obložinský, M. Sin, A. Trkov, H. Wienke, and V. Zerkina, *Nucl. Data Sheets* **108**, 2655 (2007).
- [48] M. Sin, P. Obložinský, M. Herman, and R. Capote, *J. Korean Phys. Soc.* **59**, 1015 (2011).
- [49] D. Rochman, A. J. Koning, J. C. Sublet, M. Fleming, E. Bauge, S. Hilaire, P. Romain, B. Morillon, H. Duarte, S. Goriely, S. C. van der Marck, H. Sjöstrand, S. Pomp, N. Dzysiuk, O. Cabellos, H. Ferroukhi, and A. Vasiliev, *EPJ Web Conf.* **146**, 02006 (2017).